ARL-TR-8882 ● JAN 2020

DEVCOM ARMY RESEARCH LABORATORY

Utilizing Point-Spread Functions of X-ray Sources to Increase Image Resolution of Shaped Charge Jet X-radiographs

by W Casey Uhlig and Michael B Zellner

NOTICES

Disclaimers

The findings in this report are not to be construed as an official Department of the Army position unless so designated by other authorized documents.

Citation of manufacturer's or trade names does not constitute an official endorsement or approval of the use thereof.

Destroy this report when no longer needed. Do not return to the originator.

ARL-TR-8882 ● JAN 2020

Utilizing Point-Spread Functions of X-ray Sources to Increase Image Resolution of Shaped Charge Jet X-radiographs

W Casey Uhlig and Michael B Zellner
Weapons and Materials Research Directorate, CCDC Army Research Laboratory

REPORT DOCUMENTATION PAGE

Form Approved
OMB No. 0704-0188

1. REPORT DATE *(DD-MM-YYYY)*	2. REPORT TYPE	3. DATES COVERED (From - To)
January 2020	Technical Report	1 February 2019 to 31 July 2019

4. TITLE AND SUBTITLE
Utilizing Point-Spread Functions of X-ray Sources to Increase Image Resolution of Shaped Charge Jet X-radiographs

5a. CONTRACT NUMBER

5b. GRANT NUMBER

5c. PROGRAM ELEMENT NUMBER

6. AUTHOR(S)
W Casey Uhlig and Michael B Zellner

5d. PROJECT NUMBER

5e. TASK NUMBER

5f. WORK UNIT NUMBER

7. PERFORMING ORGANIZATION NAME(S) AND ADDRESS(ES)
CCDC Army Research Laboratory
ATTN: FCDD-RLW-PA
Aberdeen Proving Ground, MD 21005

8. PERFORMING ORGANIZATION REPORT NUMBER
ARL-TR-8882

9. SPONSORING/MONITORING AGENCY NAME(S) AND ADDRESS(ES)

10. SPONSOR/MONITOR'S ACRONYM(S)

11. SPONSOR/MONITOR'S REPORT NUMBER(S)

12. DISTRIBUTION/AVAILABILITY STATEMENT
Approved for public release; distribution is unlimited.

13. SUPPLEMENTARY NOTES
ORCID ID(s): W Casey Uhlig, 0000-0003-1815-0106; Michael B Zellner, 0000-0001-7309-312X

14. ABSTRACT
A method was developed to deblur radiographs using a point-spread function acquired from the X-ray source to create sharper radiographic images with greater spatial resolution. The deblurring process includes compensation for image artifacts resulting from the X-ray generation across a finite area instead of from an ideal spot. A demonstration of the technique was performed for copper tubes and rods from less than 1 mm to 6 mm, representative of shaped-charge-jet dimensions. Radiographs resulting from the application of the point-spread function deconvolution technique and the subsequent analysis of the copper tubes and a copper shaped charge jet are presented.

15. SUBJECT TERMS
X-radiography, point spread function, deblurring, flash radiography, deconvolution, shaped charge jet

16. SECURITY CLASSIFICATION OF:			17. LIMITATION OF ABSTRACT	18. NUMBER OF PAGES	19a. NAME OF RESPONSIBLE PERSON
a. REPORT	b. ABSTRACT	c. THIS PAGE			W Casey Uhlig
Unclassified	Unclassified	Unclassified	UU	32	19b. TELEPHONE NUMBER (Include area code) (410) 278-3997

Contents

List of Figures

Acknowledgments

The authors are grateful to Dr Roarke Horstmeyer at Duke University for sharing his optical-based research and techniques, which inspired much of the research discussed here. The authors are also grateful to the members of the US Naval Research Laboratory's Pulsed Power Physics Branch within the Plasma Physics Division for collaborations and engagements concerning the X-ray source spot measurements and techniques. Finally, the authors are grateful to the technical staff at the experimental facilities of the US Army Combat Capabilities Development Command Army Research Laboratory.

1. Introduction

Radiography has been employed as a valuable nondestructive analysis tool over a broad range of fields spanning medical diagnosis[1,2] to mechanical kinematics and material diffusion.[3,4] Flash radiography[5] extends these capabilities to scientific areas requiring submicrosecond temporal resolution. This technique has been widely applied in ballistic and dynamic material response under shock loading and explosive detonations.[6,7] Recent work specifically addressed how one can increase spatial resolution of the recovered radiographic image through relatively well-known image analysis deconvolution techniques.[8] Here we apply those techniques to a shaped charge jet and test objects representative of jet dimensions.

To enhance the radiographic images, we focus on analysis methods to deblur images that have been collected using an X-ray source of a finite size. We apply our corrections assuming X-rays interact in an ideal fashion with a target object to create a shadowgraph image at the detector plane, represented using a ray-diagram approximation in Fig. 1. When a generation source is not an ideal spot, it creates an inverted image at the detector that is blurred by a factor related to the finite dimensions of the source spot and setup geometry. To correct for the finite X-ray source size, we approximate the collection system as an optical system that incurs a simplistic point-spread function (PSF). Any real X-radiographic image acquired by a non-point-like object is a convolution of the PSF with the many scattering points that make up the true object. Because of this convolution, the radiographic image undergoes both broadening of spatial features and reduction of local intensities in its raw form. However, the scattering function (image) can be recovered by performing a deconvolution.

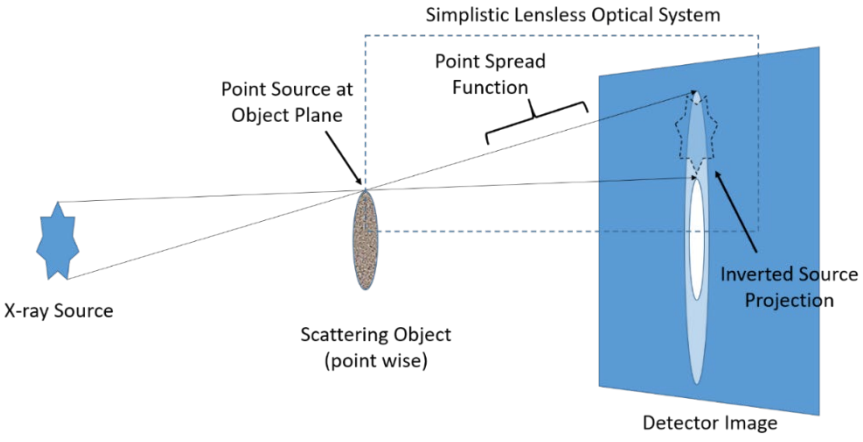

Fig. 1 Ray diagram of an X-ray collection system to a simplistic lensless optical system from a finite source[8]

The convolution process is illustrated in Fig. 2, which shows the expected radiograph profile from an ideal point source of a copper (Cu) tube of 4-mm outer diameter (OD)/0.86-mm inner diameter (ID) (Fig. 2a), the approximate profile of an actual X-ray source at the image plane (Fig. 2b)—that is, the PSF—and the convolution of the two lineouts (Fig. 2c). The transmissions are calculated using the X-ray spectrum of a 450-keV source produced by L3 Applied Technologies. The convolution is the raw signal that would be observed at the detector in an experiment. In such a case, the 4-mm rod would appear to have a width of about 6 mm, and any features such as the small hollow region of the tube would be completely obscured.

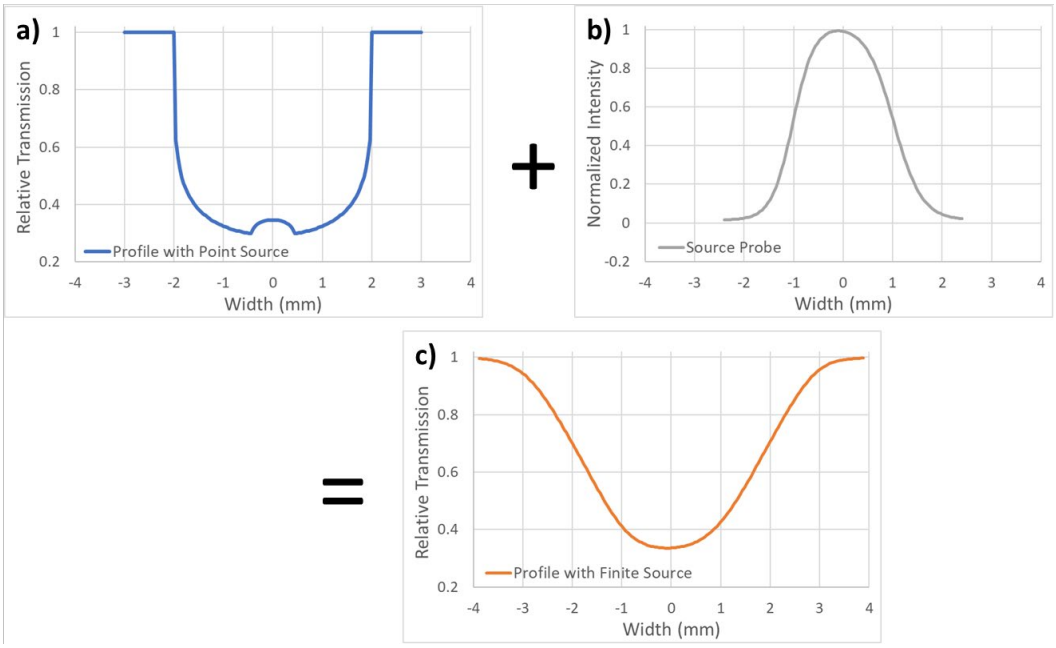

Fig. 2 Convolution process showing the predicted radiograph profile of a narrow-ID tube with 450-keV broad spectrum point source (a), a finite source profile at the image plane (b), and the convolution of the two profiles (c)

While details of the technique are outlined in Zellner and Uhlig[8], a deconvolution can be performed using the PSF and the output observed at the detection plane. The deconvolution of an image or signal from another is usually performed by a point-by-point division of the two images or signals in the Fourier domain, outlined by Norbert Wiener in 1949.[9] In practice, many data analysis software packages have deconvolution functions. Here we used the deconvolution functions available in both MATLAB[10] and Origin[11] as well as an attempt at an iterative process that used an initial guess for the object convolved with the PSF compared with the actual X-ray output. One issue that arises with using deconvolution in Fourier space is the addition of noise to the data. This is shown in Fig. 3a, where the ideal radiograph of a 4-mm OD/2.4-mm ID Cu tube is convolved with a PSF and then a

deconvolution is performed with the Origin "deconv" function using the identical PSF. While the shape is recovered well, significant noise is generated. The Wiener deconvolution method includes a term related to the signal-to-noise levels to counteract inherent output noise. This noise-to-signal ratio is included in the MATLAB "deconvwnr" function, which we will simply refer to as the noise term or noise level. Figure 3b includes deconvolutions for three different noise levels. As the noise term is increased, the output is smoother but the effectiveness of recovering the original signal decreases. For the convolution and deconvolution in Fig. 3, the noise level is very low because the input data are generated from calculations, thus the deconvwnr function recovers the original profile well with limited output noise.

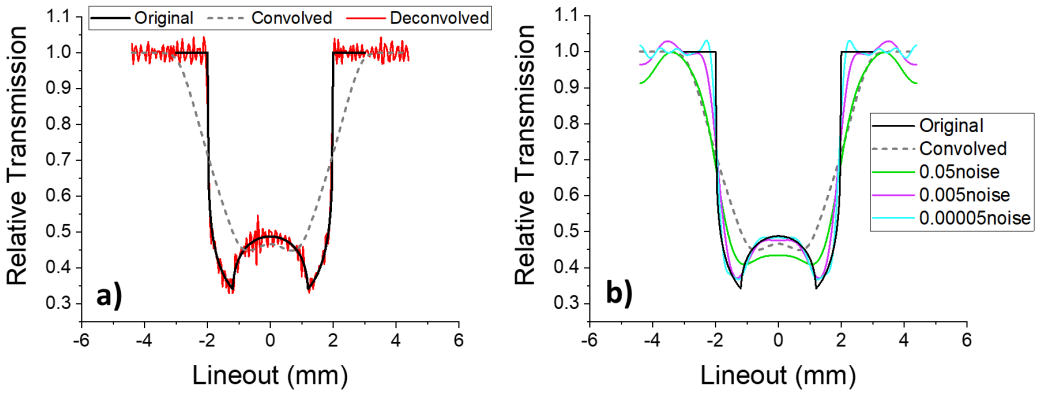

Fig. 3 Convolution and deconvolution of a Cu tube's X-ray profile illustrating the inherent noise

As was done in Zellner and Uhlig,[8] the PSF for the experimental work included here was attained by imaging the 450-keV X-ray source using a pinhole in a lead sheet at the object plane. Two pinholes of different sizes (1.2 ± 0.1 mm and 0.4 ± 0.1 mm) were used in attempting to obtain a good approximation of the actual PSF. The resulting images and profiles across the center of the peak intensity of the source are shown in Fig. 4. The X-ray tube head to shot line (object plane) distance (x_1) was 28.0 inches (711.2 mm), while the shot line to detector surface distance (x_2) was 17.5 inches (444.5 mm) yielding a magnification factor of 0.625 in the pinhole camera configuration and 1.625 for the object radiograph configuration. Based on the images of Fig. 4, the source spot size would be approximately 6.7 to 7.3 mm, whereas the source as measured in Zellner and Uhlig[8] was 6.5 to 6.7 mm, thus fairly similar.

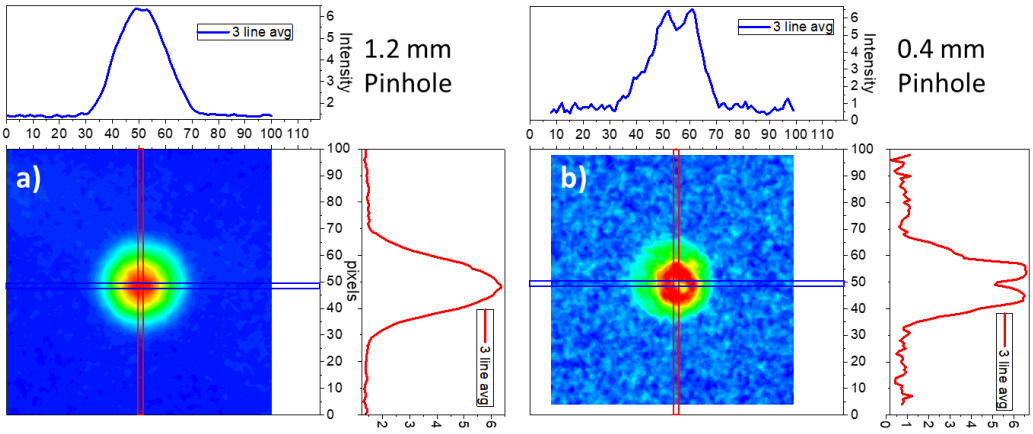

Fig. 4 Pinhole images acquired for determining the PSF of the 450-keV X-ray source used for the radiographs

However, there is inherent blurring due to the finite size of the pinhole. If our source is a disc of radius r_1, then a projection through a true point-like pinhole would have a radius of r_2, where $r_2 / r_1 = x_2 / x_1$. Through a nonideal pinhole of diameter D, a projection expanding to radius h would be observed as illustrated in Fig. 5. From triangle ABC in the illustration, we get

$$\frac{h + r_1}{x_1 + x_2} = \frac{D/2 + r_1}{x_1}.$$

Thus,

$$h = \frac{D}{2}\left(1 + \frac{x_2}{x_1}\right) + r_1 \frac{x_2}{x_1},$$

$$r_1 = -\frac{D}{2}\left(1 + \frac{x_1}{x_2}\right) + h \frac{x_1}{x_2},$$

and

$$r_2 = h - \frac{D}{2}\left(1 + \frac{x_2}{x_1}\right).$$

The actual source dimension r_1 can then be calculated from the observed image at the detector with dimension h, and the source image can be reduced to the true PSF dimension by calculating r_2. For our pinhole geometry, we calculate that the PSF needs to be reduced by a factor of 1.22 and 1.08 from the pinhole images of Fig. 4a and 4b, respectively.

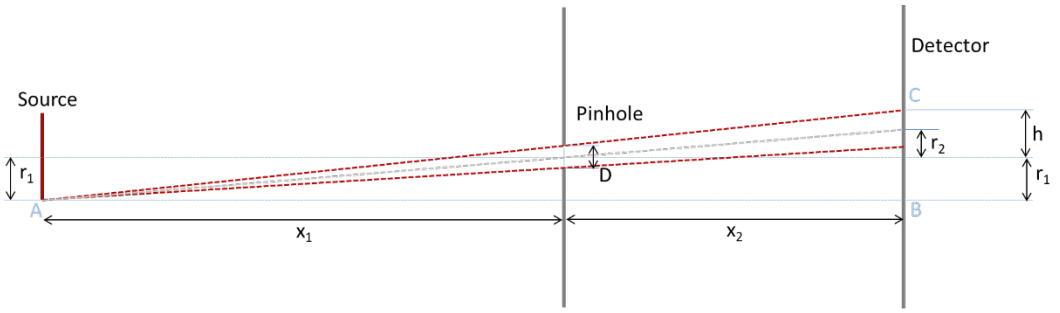

Fig. 5 Ray diagram of pinhole camera setup illustrating inherent blur due to pinhole size

Uncertainty remains in how to best reduce the PSF. Is it better to shrink/narrow the entire function uniformly, or is it more realistic to simply trim the edges? Figure 6 shows the projection profile from the 1.2-mm pinhole with an asymmetric double Sigmoidal fit reducing the total width of the profile by 1.22 while maintaining the width at 68% of max intensity. Figure 7a shows the convolution of the predicted point source radiograph of the 4-mm OD/2.4-mm ID Cu tube with reduced width fit of Fig. 6 as the PSF. This is directly compared to the profile of the actual 450-keV X-ray. The same comparison is made in Fig. 7b using the pinhole projection reduced uniformly by 1.22 times as the PSF for convolution. The edge-reduced method seems to have a better prediction of the convolution occurring in the actual radiograph, while the uniform reduction yields too high of fidelity of the object features. Likely, reducing the PSF uniformly narrows the peak intensity too much, which leads to decreased convolution and thus is less effective for the deconvolution of the actual radiographs. Additionally, since any blurring would only add a minor intensity increase to the whole of the PSF, the blurring is most noticeable where the value of the PSF is low (i.e., at the wings). So using the edge reduction seems to be the most physically appropriate.

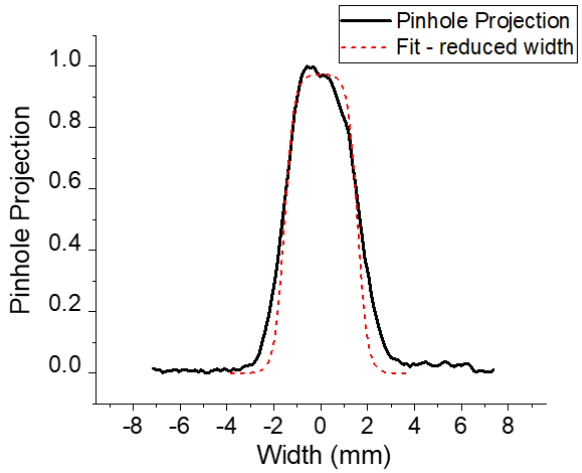

Fig. 6 Profile of the 1.2-mm pinhole projection and reduced edge fit

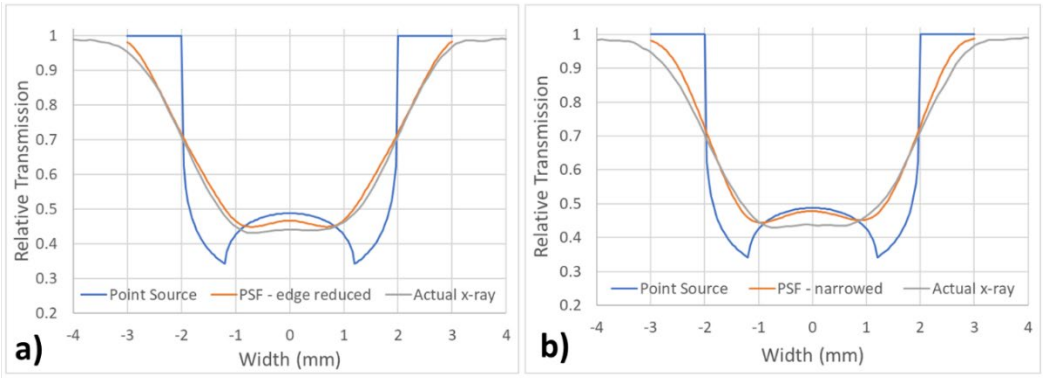

Fig. 7 Radiographic profile of a Cu tube compared with the predicted profile convolved with PSFs as adjusted from the pinhole projections

2. Deconvolution of X-radiographs of Copper Tubes and Rods

Four PSFs derived from the small pinhole (0.4 mm) projections in addition to the reduced edge fit from Fig. 6 were chosen to perform deconvolutions on the radiograph profiles of Cu tubes and rods. This analysis provided a baseline understanding of the limits of this experimental setup to extract data from a shaped charge jet of similar dimensions. Because the small pinhole projection is closer to the actual PSF, a multipeak fit of the entire projection without width reduction, as shown in Fig. 8a, was chosen. Additionally, a direct uniform reduction in size of the multipeak fit by a factor of 1.08 (or squished PSF), a double-peak fit with reduced PSF edges (by 1.08 at the profile base), and a single-peak fit with reduced PSF edges (by 1.08 at the profile base) were tested as potential PSFs and are shown in Figs. 8b, 8c, and 8d, respectively. The squished multipeak fit of Fig. 8b is compared to the original multipeak fit for direct comparison (instead of the projection) and has a higher peak intensity because the PSFs need to be normalized to unity (i.e., the sum across the entire PSF needs to be 1). The edge-reduced PSF from the 1.2-mm pinhole projection is also shown in Fig. 8d to compare to the edge-reduced single-peak fit of the 0.4-mm pinhole projection. In this case, the two PSFs should be very similar (and, in fact, they are).

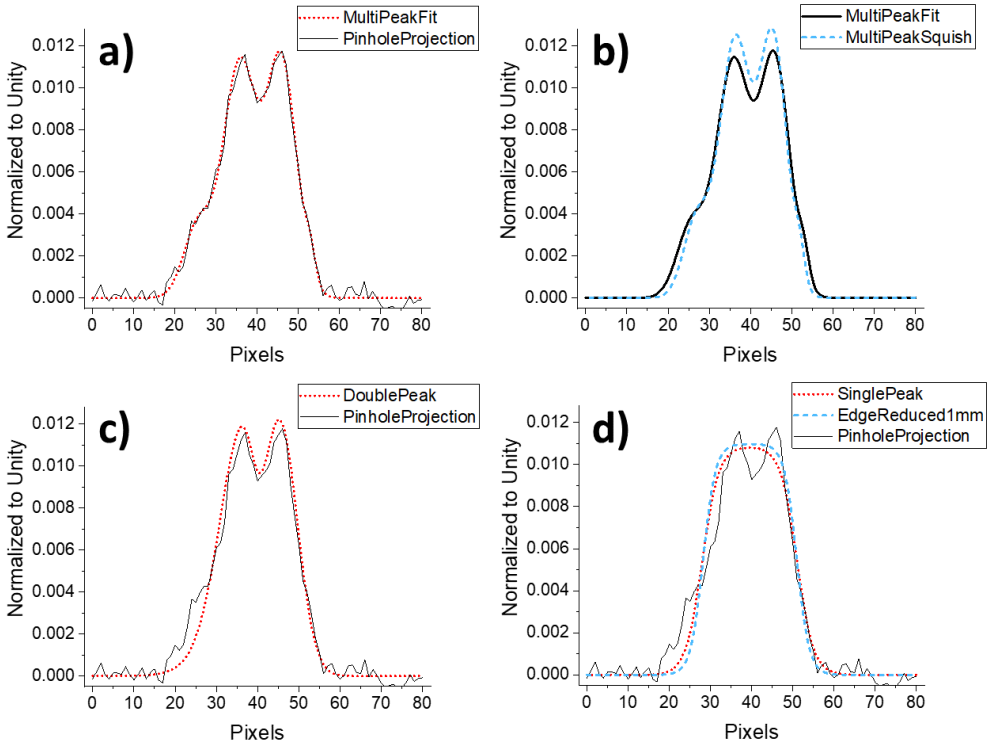

Fig. 8 Various PSFs based on the small pinhole projections of the 450-keV X-ray source

Wiener deconvolution was performed on the radiograph profile of the 4-mm OD/ 2.4-mm ID Cu tube using all five of the PSFs. The resulting approximations for the object via "deconvwnr" with a noise factor of 0.005 are shown in Figs. 9a–9d along with the original radiograph lineout for comparison. The deconvolutions utilize the PSFs in Figs. 8a–8d, respectively.

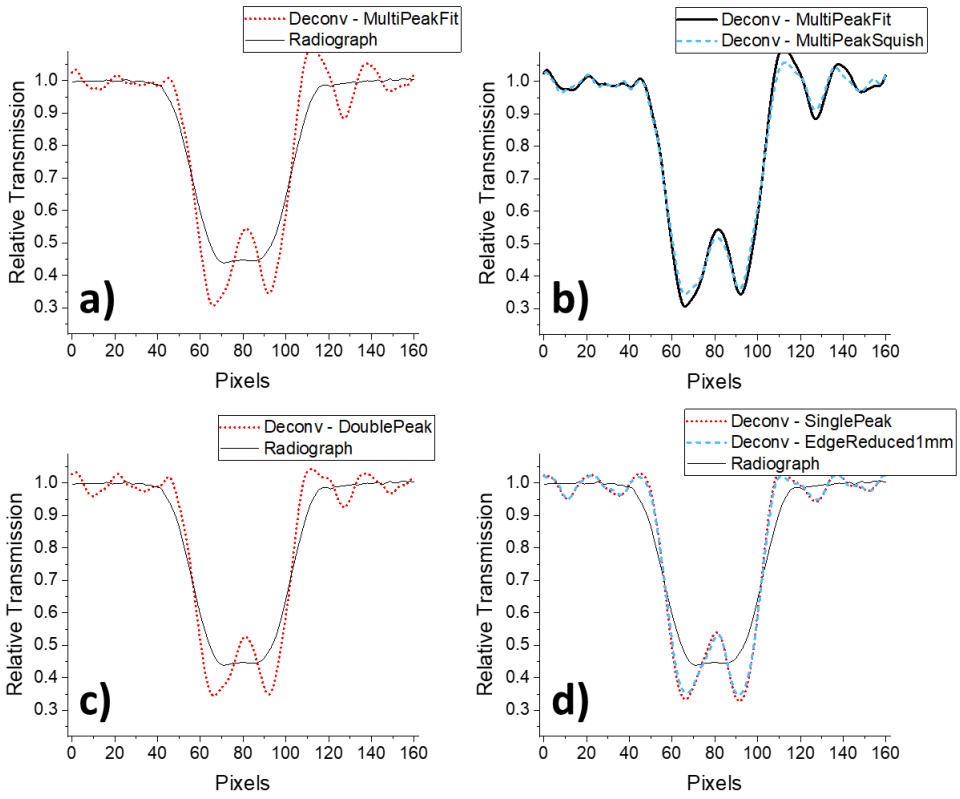

Fig. 9 Deconvolutions of the Cu tube radiograph lineout from the PSFs in Fig. 8

Figure 9b shows the deconvolution for both the multipeak fit and the multipeak fit-squished PSFs for a direct comparison in the effect of reducing the PSF total width by the factor of 1.08.

Four facts are readily apparent:

- Recovery of the hollow feature (as is observed in an ideal radiograph of a tube) is well above the baseline noise level (baseline defined as regions away from the tube, nominally a relative transmission of 1).
- The baseline noise level is significantly increased during deconvolution, particularly at a sharp edge feature/transition. The average standard deviation of the baseline on the deconvolved lineouts is 0.022, while the average hollow/tube feature has a peak-to-peak signal (as determined by the local maxima at the center and the second minima) of 0.17 for the five deconvolution test cases.
- The width of the Cu tube profile in the lineout narrows considerably as expected.
- There is not a considerable difference in the results from the differing PSFs.

Defining the signal-to-noise ratio (SNR), which in this case is the feature-to-noise ratio, as the peak-to-peak of the hollow feature divided by the standard deviation of the baseline (σ), we get values of 6.32, 7.03, 8.05, 8.25, and 8.39 using the PSFs from the multipeak fit, multipeak fit-squished, double peak, single peak (0.4-mm pinhole), and edge-reduced fit (1.2-mm pinhole), respectively. While σ of the original radiograph is much lower, 0.005, the SNR is only 1.86, a factor of 4 lower than the deconvolved SNR.

Concerning the measurement of the Cu tube's diameter via the radiograph, the width of the profile at 2σ (average from the deconvolved baseline noise for consistency in comparison) below baseline is 68.9 pixels (5.89 mm) for the original radiograph, while the deconvolved profiles average a width of 56.25 pixels (4.81 mm). Of course, the ideal is 4 mm, and the deconvolution results are still too wide; however, the deconvolution does eliminate 22.5% of the overestimate in width (and 50% by volume assuming a cylindrical geometry, which we have in this case) relative to the original radiograph. That said, the ideal, the original, and the deconvolved radiographs all merge at full-width-half-max at a value in the range of just greater than 3.9 mm.

Figure 10 shows the deconvolution results compared to the lineout of the calculated ideal point source radiograph from Fig. 7. The PSFs with significant asymmetry, like the multipeak fit and double-peak fit, cause an asymmetry in the resulting deconvolution. Based on a slight asymmetry in the hollow-feature region observed in the original radiograph, there should exist some asymmetry in our source and thus a resulting PSF. However, the asymmetry in the 0.4-mm pinhole image must be excessive based on the deconvolution results (and is definitely more pronounced than the asymmetry observed in the 1.2-mm pinhole projection). This may be due to uncertainty in the feature size of the pinhole (a 0.4-mm drill bit into a 1-mm lead sheet is the limit of our manufacturing capability and any flaws may have exaggerated the asymmetry), or it may likely be shot-to-shot variation in the X-ray formation at the source (the source cannot be measured simultaneous to the acquisition of the radiograph, and there may have been less asymmetry in X-ray generation for the flash used for the Cu tube's radiograph). Regardless, slightly lower asymmetry as in the two single-peak PSFs yields the best deconvolution match to the ideal and the best SNRs.

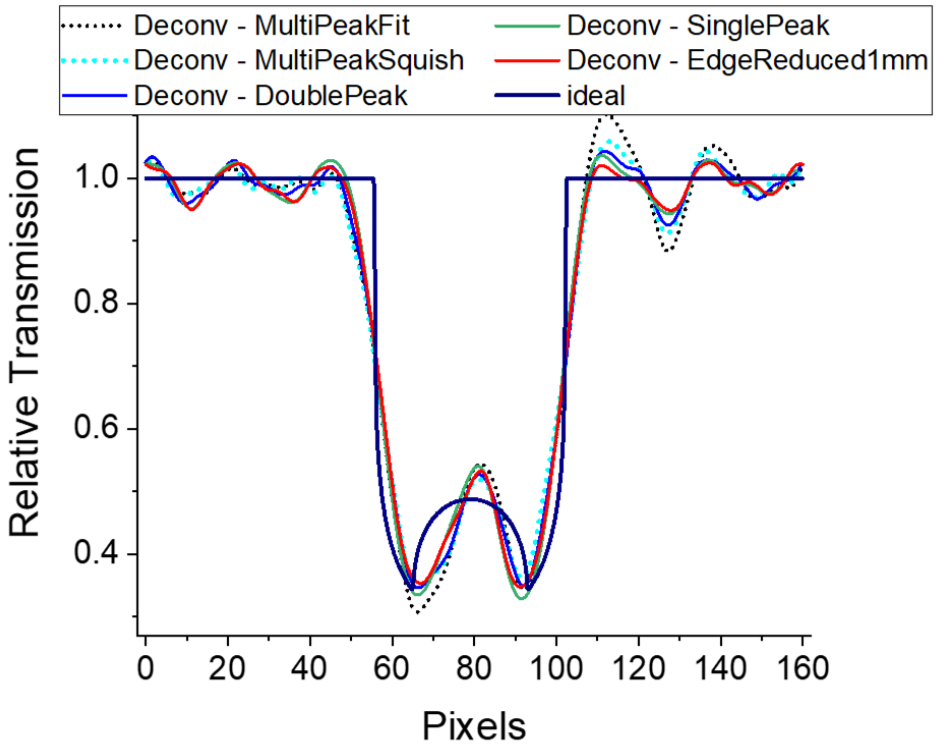

Fig. 10 Wiener deconvolutions of the Cu tube's lineout compared with the calculated ideal point-source radiograph

An attempt to deconvolve the radiograph lineout via an iterative process was also made to investigate the potential to reduce the noise. An initial guess or approximation of the radiographed object was made (this can be the radiograph to begin with), which is then convolved with one of our measured PSFs. The resulting approximate output image is compared to the radiograph, and a new guess is made for the object. The process is repeated until the output image matches the radiograph. This is illustrated in Fig. 11. The results using the single-peak fit PSF are shown in Fig. 12. The final approximate image is a very nice representation of the radiograph, and the final approximate object does look quite similar to the other deconvolutions. Nevertheless, the SNR is 7.74 and is not an improvement over the Wiener deconvolution using Fourier analysis. The deconvwnr function result is shown for a direct comparison, which has an SNR of 8.25.

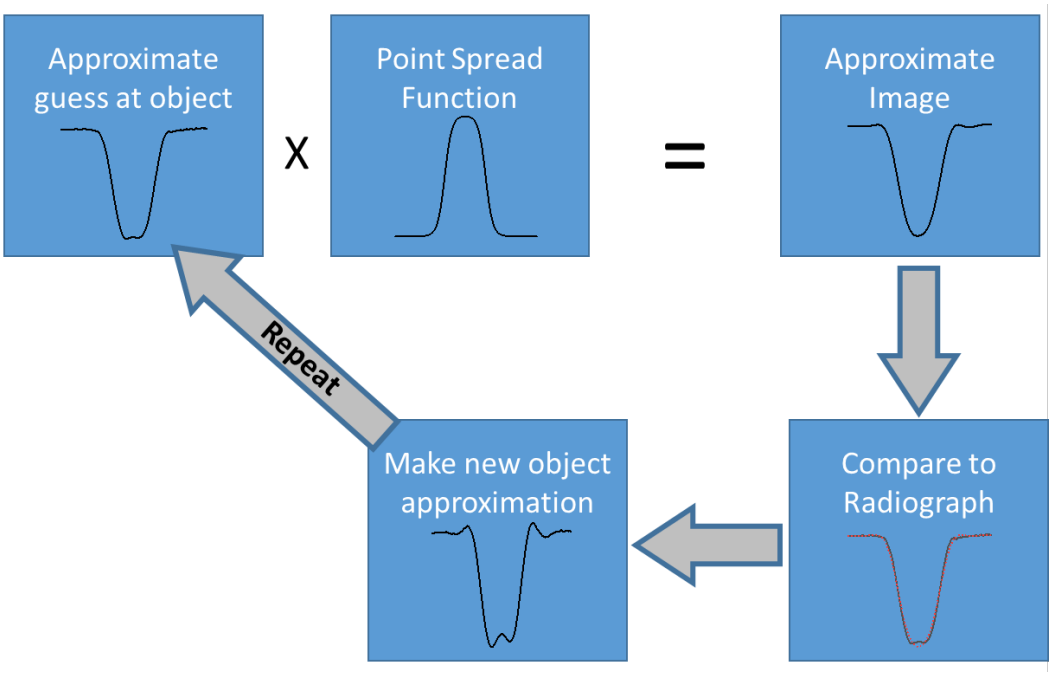

Fig. 11 Iterative deconvolution process

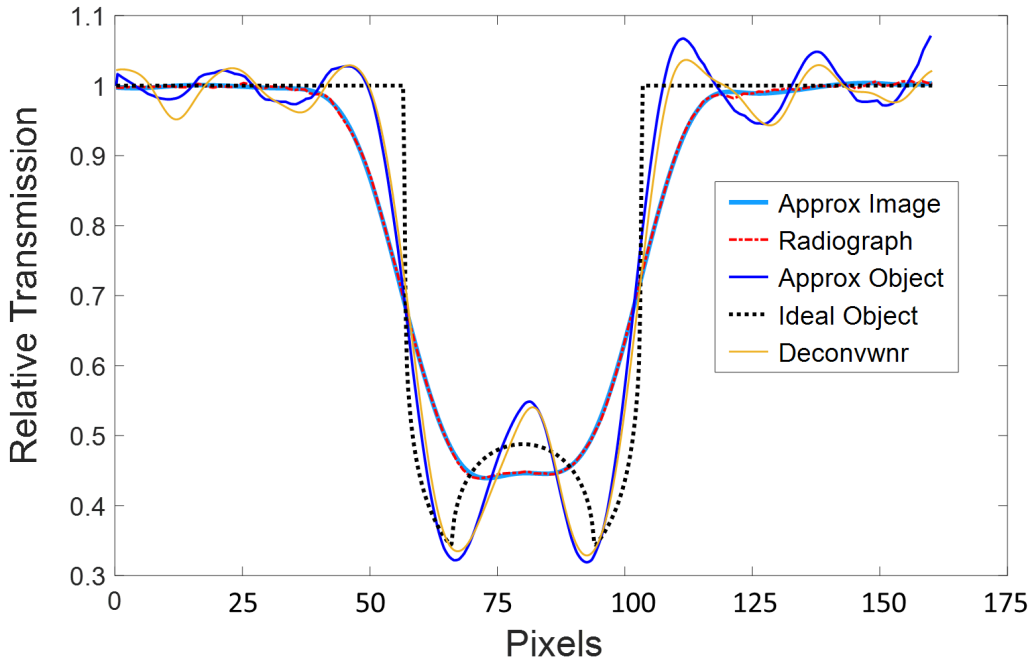

Fig. 12 Iterative deconvolution of the Cu tube's lineout compared with the calculated ideal point-source radiograph and the Wiener deconvolution function results; final approximate image and original radiograph are also compared

3. PSF Choice for Image Deconvolution

Because less asymmetry in the PSF proved beneficial for the lineout comparisons, 2-D symmetric PSFs were generated to approximate the small pinhole image. A PSF composed of discrete discs of varying intensity was generated as shown in Fig. 13a. Smoothing was performed on the discs to generate a second PSF (Fig. 13b) to compare more qualitatively with the 0.4-mm pinhole image PSF shown in Fig. 13c. Lineouts of the pixel intensity across the images horizontally are shown directly below the PSFs in the figure. The dimensions of the pinhole image were reduced by a factor of 1.08 uniformly across the image to generate the PSF.

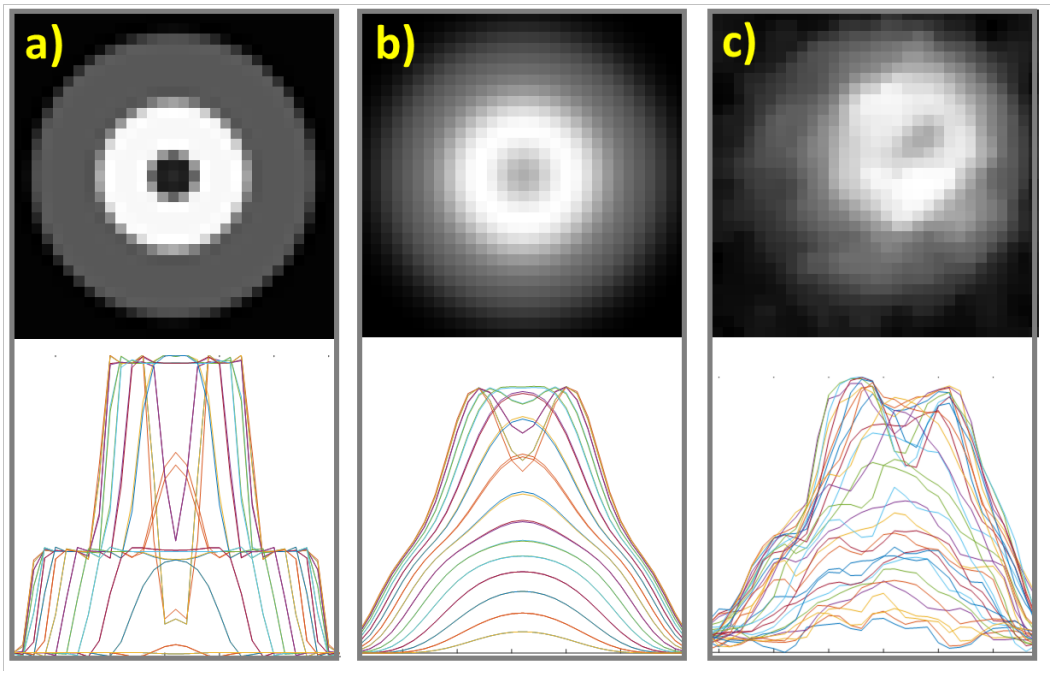

Fig. 13 2-D PSFs used for image deconvolution: discs of varying intensity (a) and the same discs smoothed (b) were used to represent the pinhole image (c); lineouts are shown directly below the images to assess the image profile

Wiener image deconvolution was performed using the PSFs on the Cu tube and rod fiducials, as well as a Cu step wedge and an optical slit fiducial using a noise factor of 0.005. The original radiograph is shown in Fig. 14a with the diameter of each rod or tube component labeled in millimeters. Only the farthest-right set of cylindrical objects are composed of interconnecting tubes; the others are stepped cylinders or rods. The ID of each tube is matched to the next smallest tube step, with the final tube (1.6-mm OD) having an ID of 0.8 mm. The optical fiducial has slits of 10.0, 2.0, 1.0, 0.75, 0.50, 0.40, 0.33, 0.25, and 0.17 mm. The images in Figs. 14b and 14c result from the deconvolution using the multidisc PSF (Fig. 13a) and the pinhole image PSF (Fig. 13c), respectively. There was no significant differences

observed between the multidisc PSF and the smoothed disc version. Therefore, the images compared in the remainder of the report will only show the multidisc and pinhole PSF results. Both deconvolutions significantly sharpen the radiograph.

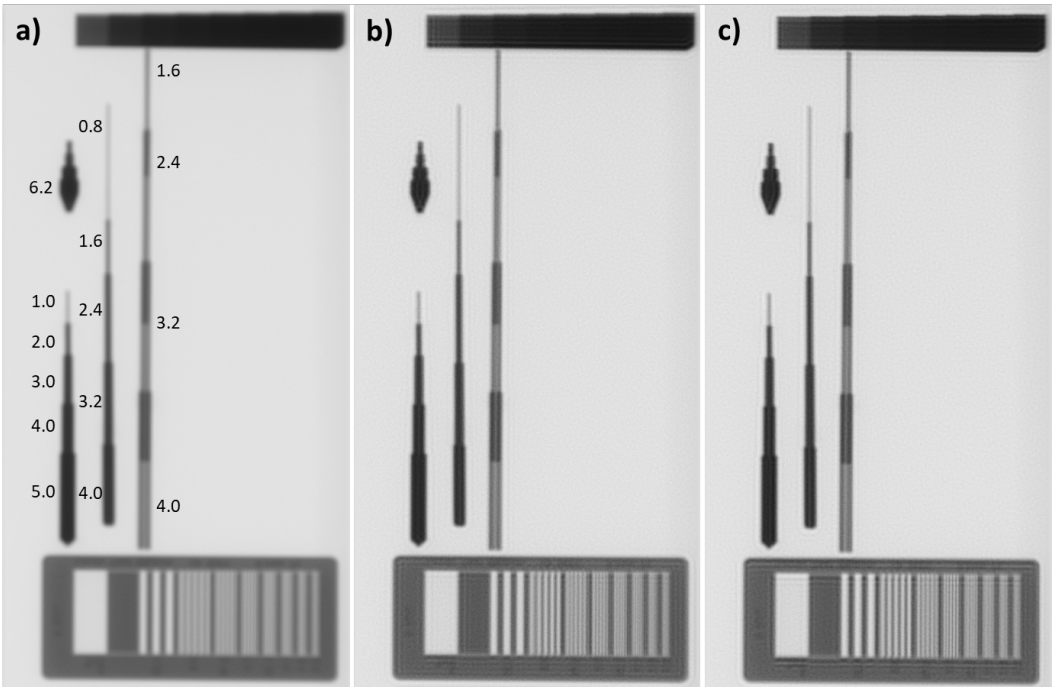

Fig. 14 Original radiograph of the fiducials (a) compared with deconvolution results using the multidisc PSF (b) and the pinhole image PSF (c)

Figure 15 shows a magnified view of the optical slit fiducial of the original radiograph (Fig. 15a), multidisc PSF result (Fig. 15b), and pinhole image PSF result (Fig. 15c). From the 1-mm slit set to the 0.17-mm slit set, a total of five slits per set should be observable in an ideal point-source radiograph. The smallest slits with a 1.625 magnification should cover 0.28 mm or 2 pixels on our detector. For the original radiograph, only four of the 0.75- and 0.50-mm slits are observable, and conclusive distinction of slits at widths below 0.50 mm is not tenable. Slits in the multidisc PSF deconvolution are detectable down to 0.33 mm (approximately 4 pixels), where all five slits are distinguishable. While the pinhole PSF creates a much sharper image with more distinct and higher contrast transitions at 0.50-mm slits than the multidisc PSF, not all five of the 0.33-mm slits are distinguishable.

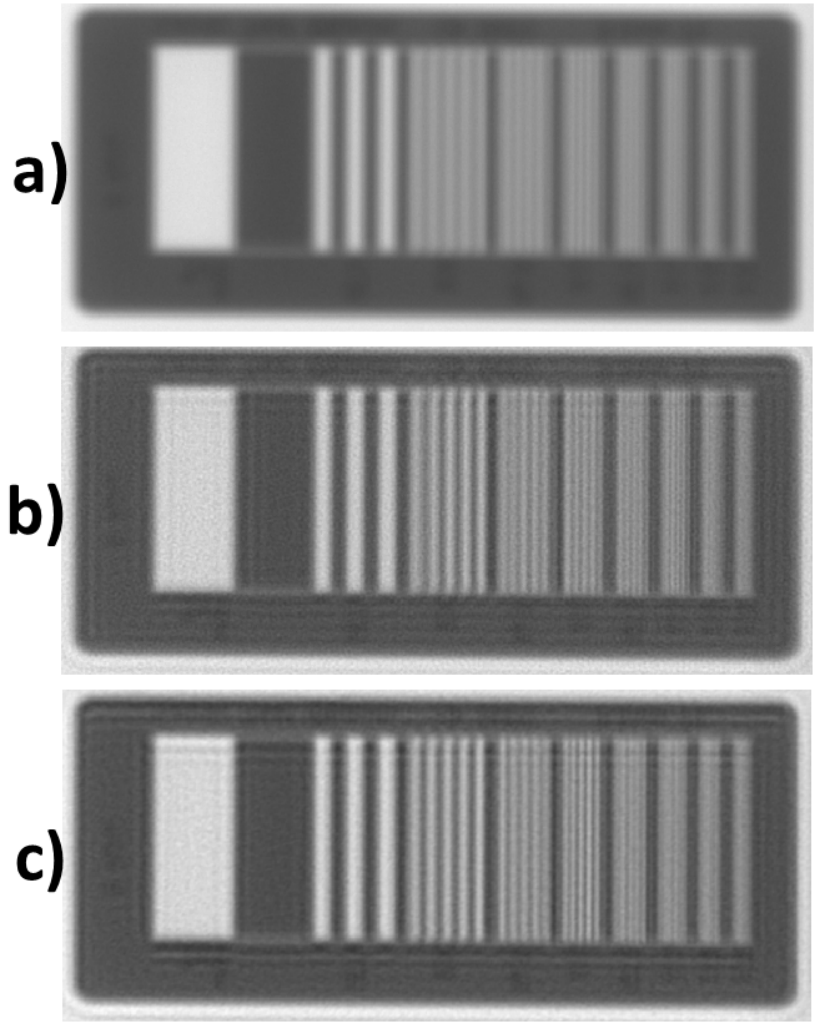

Fig. 15 Zoomed-in view of radiographs of the optical sensor, which has slits of 10.0, 2.0, 1.0, 0.75, 0.50, 0.40, 0.33, 0.25, and 0.17 mm, including the original radiograph (a), the multidisc PSF adjusted image (b), and the pinhole PSF adjusted image (c)

The marked improvement in image resolution is highlighted by a lineout shown in Fig. 16, which directly compares the original radiograph with the deconvolved image using the pinhole PSF. The lineout covers the region crossing the 2.0-mm slits down to the 0.17-mm slits, with a zoomed-in section (blue box) emphasizing the 0.75-, 0.50-, and 0.40-mm slits. All five 0.50-mm slits from the deconvolved image's lineout are clearly distinct, with much greater intensity contrast than available in the original radiograph. The average relative intensity in the region of the 0.5-mm slits is 0.672 and 0.676 for the original and pinhole PSF deconvolved images, respectively, with average intensity fluctuations across the slits of 0.026 and 0.141 (thus, contrast changes of only 4% in the original radiograph, and nearly 21% for the pinhole PSF deconvolved image).

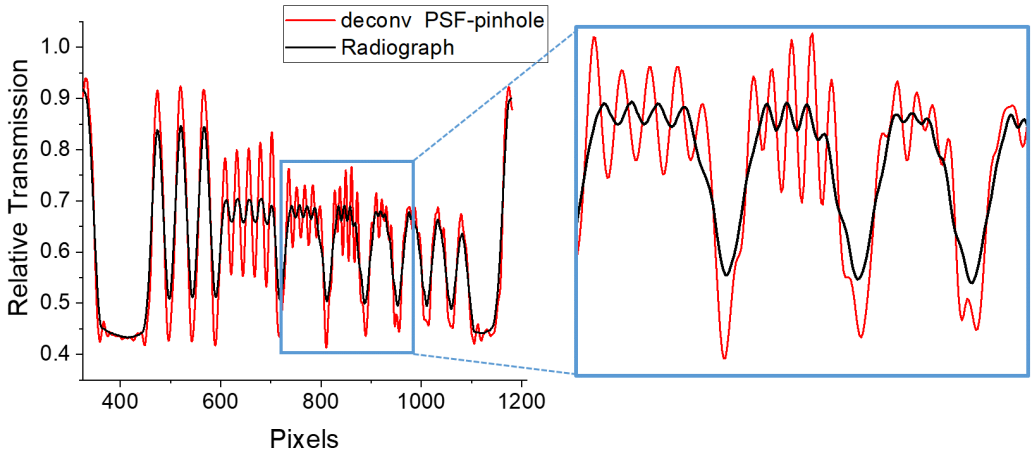

Fig. 16 Lineouts of the original radiograph and pinhole PSF deconvolved image of the optical slit fiducial

Figure 17 shows a magnified view of the Cu rod and tube fiducials of the original radiograph (Fig. 17a), multidisc PSF result (Fig. 17b), and pinhole image PSF result (Fig. 17c). The "hollow" feature of the tubes is visible in the deconvolved images down to the 3.2-mm OD/1.6-mm ID section of the fiducial. This feature is only detectable in the 4.0-mm-diameter sections of the tubes in the original radiograph. Lineouts were taken across the rods and tubes at the locations labeled 1 (crossing the 4.0-mm-diameter solid rod, 3.2-mm-diameter solid rod, and the 4.0-mm OD/ 2.4-mm ID tube) and 2 (crossing the 6.2-mm-diameter solid rod, 0.8-mm-diameter solid rod, and the 2.4-mm OD/1.6-mm ID tube) in green in Fig. 17a. Because our source-spot size is similar in dimension to the rod diameter, the noise generated by the deconvolution process has a periodicity similar to the rod diameter. Thus, a feature that is similar to that of the hollowness of a tube is generated in the rod data. This feature is on the same order in magnitude of the noise at the edge transitions of the material. This is clearly observable in Fig. 18a for the lineout associated with Location 1, particularly for the 4-mm-diameter rod.

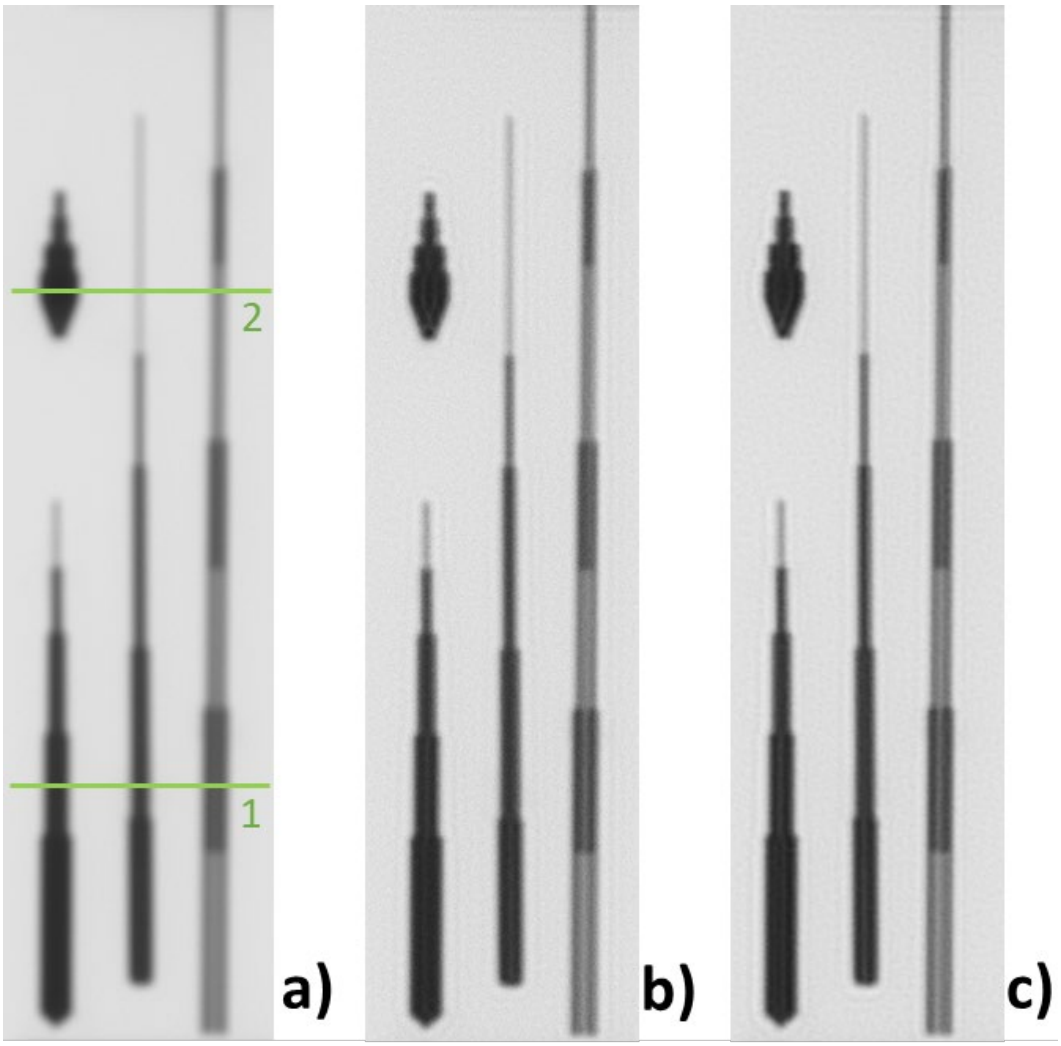

Fig. 17 Zoomed-in view of radiographs of the rod and tube fiducials, including the original radiograph (a), multidisc PSF adjusted image (b), and pinhole PSF adjusted image (c)

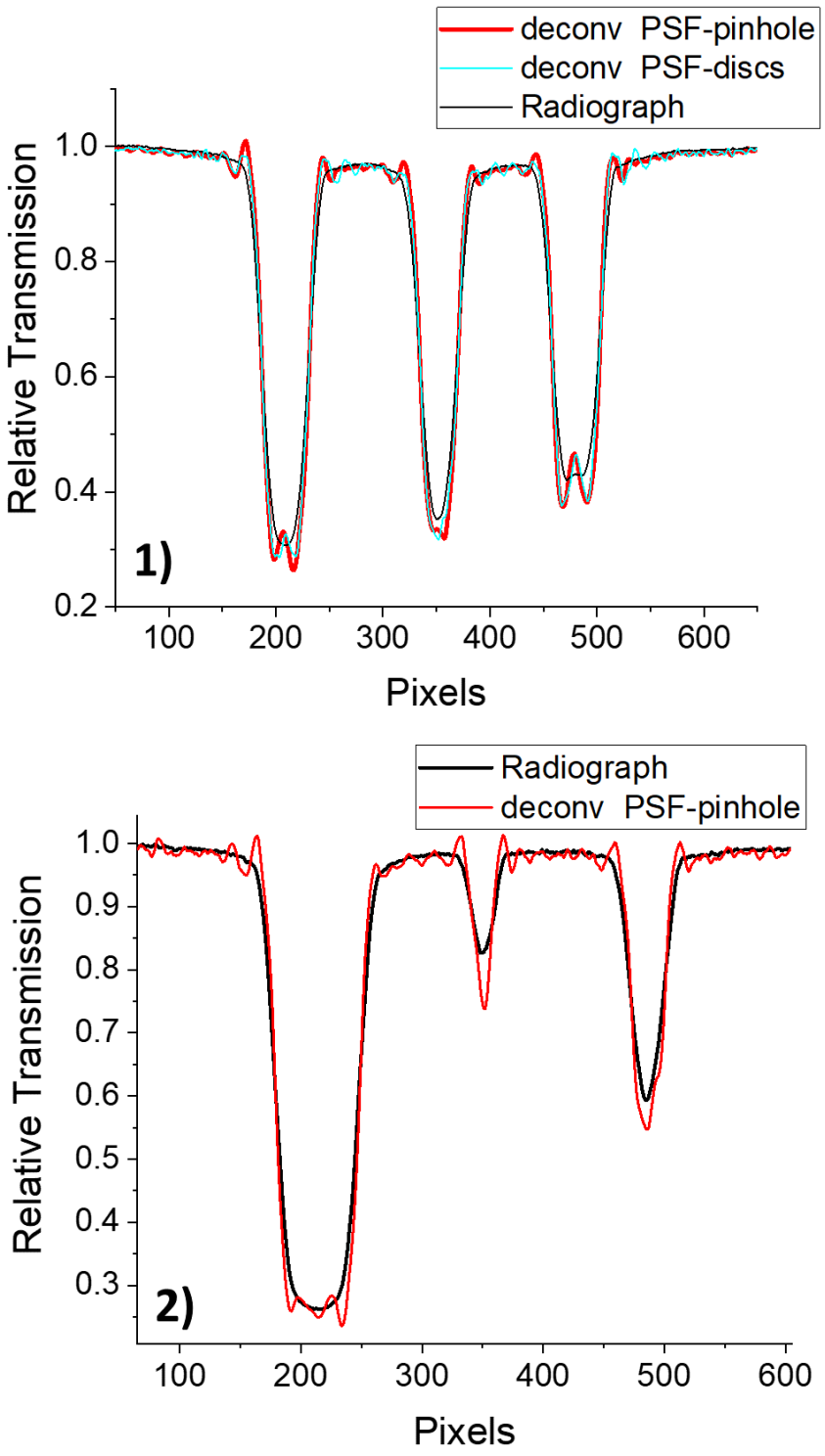

Fig. 18 Lineouts from fiducial images at Locations 1 and 2 as indicated in Fig. 17

For the multidisc PSF deconvolved image, the SNR is 5.3 for the 4.0-mm tube and 2.7 for the 4.0-mm solid rod (assuming the same analysis as the tubes in Section 2 of this report) in the lineouts of Fig. 18 (Part 1). The peak-to-peak signal (from the

center of the rod or tube)/peak-to-peak noise at the material edge is 2.14 for the tube and 1.05 for the rod. Essentially, this confirms that the hollow tube feature observed for the actual tube is outside the noise, while the similar artifact on the rod is within the noise. This is more clearly illustrated visually with the wider rod. Figure 18 (Part 2), which contains the lineout from Location 2, shows that the rod with a diameter of 6.2 mm has multiple noise ripples and not hollow-type features.

The lineouts also allow quantification of the smaller features. The 0.8-mm-diameter rod appears to have a full width of 3.0 mm. With deconvolution, the width is reduced to 2.2 mm. A significant reduction, but still well above the actual size (even full-width-at-half-max on the deconvoluted image is 1.2 mm). Alternatively, the deconvolved radiograph of the 6.2-mm-diameter rod has a full-width-at-half-max of 70.2 pixels or 6.0 mm. In Fig. 18 (Part 2) the 2.4-mm OD/1.6-mm ID tube has a full-width-at-half-max of 2.5 mm. Thus, features at this scale begin to be reliably measured. It also appears to have some noticeable features associated with the hollow region when utilizing the deconvolution. Figure 19 is a more detailed look at the lineout for the 2.4-mm tube. While we know the hollow region exists, it is impossible to determine the feature with any certainty because it is within the background noise (SNR 1.1). However, the 3.2-mm OD/1.6-mm ID tube had an SNR of 4.4, which is above the type of signals observed in the solid rod. Thus, the smallest hollow feature actually detected is 1.6 mm but is not repeatable for all OD tube sizes.

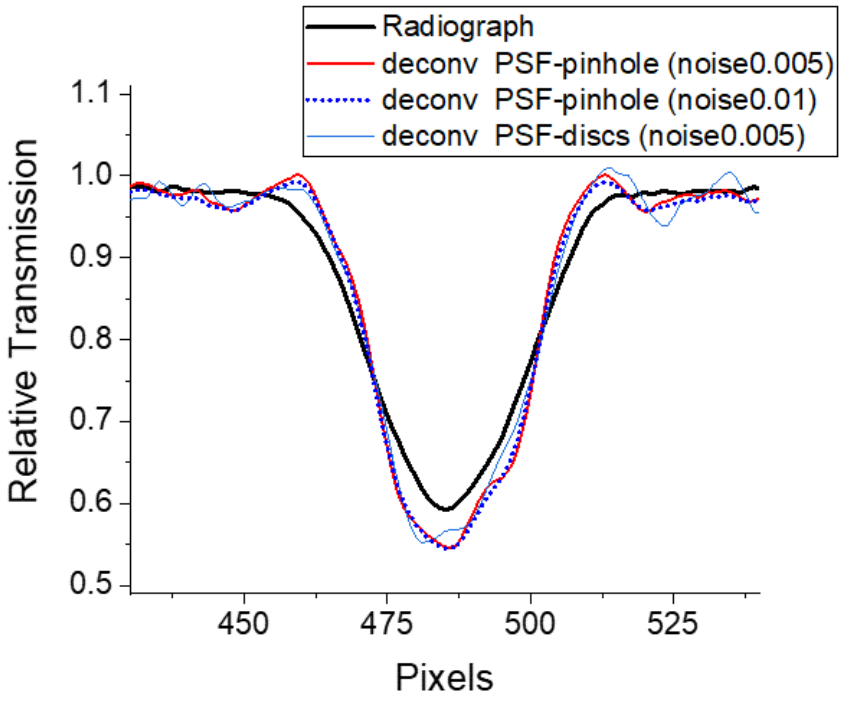

Fig. 19 Lineout of the 2.4-mm OD/1.6-mm ID Cu tube

4. Shaped Charge Jet

A 65-mm-diameter Cu shaped charge was detonated such that the jet was formed on the same shot line as the Cu tube and rod fiducials (724-mm standoff from warhead to jet tip at X-ray flash). The jet forms a tip with a nominal diameter of 4 to 5 mm and length of 15 to 20 mm. Behind the tip, a typical diameter of 2 to 3 mm is expected at this standoff. Figure 20a shows the unmodified radiograph of the jet. Details of the jet including separation as the jet particulates, small particles surrounding the jet, and a melted leading rod protruding from the front of the tip, which are typical of this round, are quite blurred. Figures 20b and 20c compare deconvolution-processed images. Because there is very little difference between the results of the differing PSFs, images obtained using two different noise term settings in the deconvolution are compared in Fig. 20 for the multidisc PSF and not two different PSFs. Qualitatively, the contrast is enhanced (as in the fiducial X-rays), revealing some features as noted previously. More importantly, particle size is more distinct. For instance, a lineout of the diameter of the seventh particle exhibits a difference of 3.2 mm in the original radiograph versus 2.6 mm for the deconvolved image, revealing a 50% overestimate in particle mass. (This is within the feature size reliably measured with the deconvolution process for the fiducials in Section 3.) For the lead particle the difference is 5.5 mm versus 5.0 mm, closer but still nearly 20% mass difference. These lineouts are shown in Fig. 21.

Additionally, particle separation becomes more distinct. A lineout along the length of the jet illustrates this in Fig. 21, with lineouts for the original, deconvoluted with noise term 0.0025, and deconvoluted with noise term 0.01. The location the lineouts were obtained are shown on the included image (which is the original radiograph). This gives some insight to the necking down during particulation. The gap between particles or the second peak in the horizontal line scan for the original is 2.6 mm, while the deconvolved image has a gap of 2.4 mm. The overall transmission is also significantly lower along the jet in the deconvoluted images, signifying the potential of more material in the necked-down regions than what would be concluded from the original radiograph.

Analysis analog to that of the tube and rod in Section 3 reveals an SNR of 4.4 on the lineout of the jet tip (from the deconvolution with the noise term set to 0.01). The peak-to-peak signal (or inflection from the center of the jet)/average peak-to-peak noise at the material edge is 1.17 for the same lineout. While the SNR is on par with our smallest detected hollow regions in the tube, the peak-to-peak signal is only slightly larger than the rod (1.09). Inspection of the data shows large noise inflections at one edge and very moderate at the other. Thus, it is difficult to draw

any conclusions concerning the jet composition and potential voids based on the radiograph obtained in this setup.

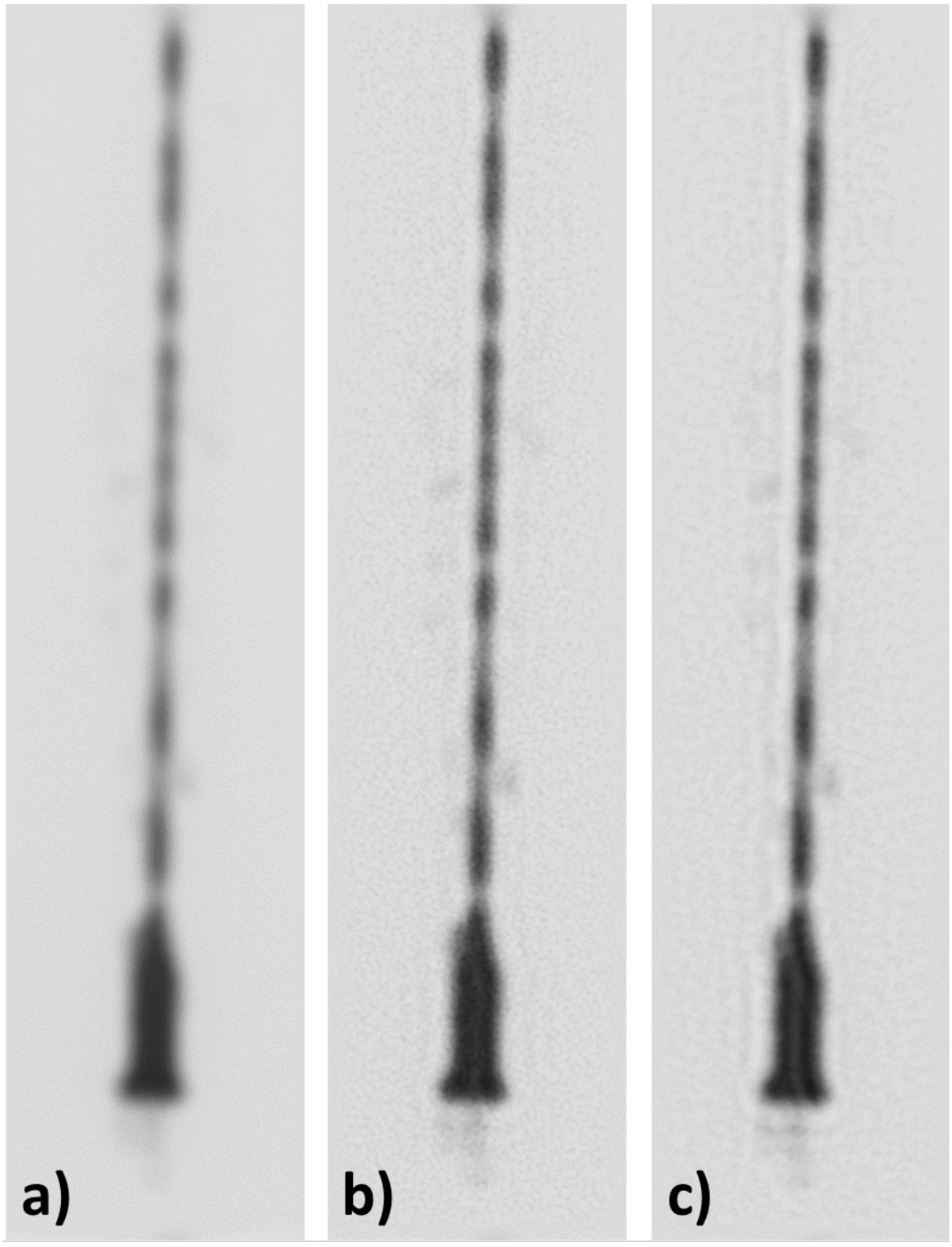

Fig. 20 Radiograph of a Cu shaped charge jet (a) compared with a multidisc PSF adjusted image with the deconvolution noise term set to 0.005 (b) and 0.01 (c)

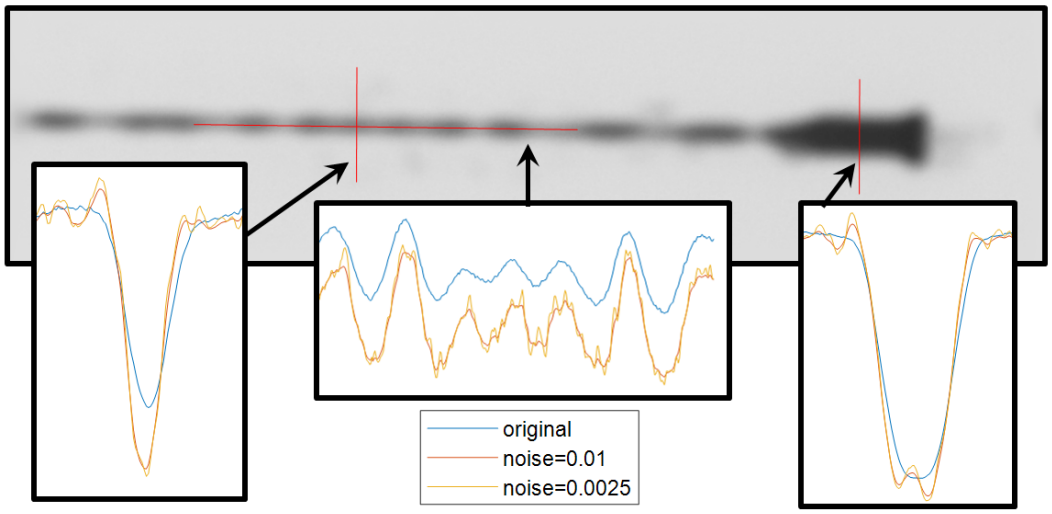

Fig. 21 Lineouts of jet diameter at two particle locations as well as along the length of the jet to determine particle separation

5. Conclusions

PSFs were ascertained for a 450-kV X-ray setup and tested on fiducials indicative of dimensions and features of a shaped charge jet. Hollow features in tubes were characterized, and limitations to the deconvolution process were determined. Hollow features on the order of 1.6 mm were detectable for this system. The frequency of the noise induced by the deconvolution happened to be at about half the thickness of the rod diameters of interest for shaped-charge-jet study, causing inflections in the data, which would otherwise be indicative of a hollow feature. Thus, careful comparison to induced noise and feature size is required.

A shaped charge jet was imaged with the 450-kV radiograph setup and analyzed using the information developed from the fiducial image processing. Significant contrast enhancement and detection of particle features were enabled using the deconvolution process. This showed a significant overestimate in mass of some of the particles if the original radiograph alone was used for analysis.

6. References

1. Doi K. Diagnostic imaging over the last 50 years: research and development in medical imaging science and technology. Phys Med Bio. 2006;51(13).

2. Pines JM. Trends in the rates of radiography use and important diagnoses in emergency department patients with abdominal pain. Med Care. 2009;47(7):782–786.

3. Kastengren AL, Tilocco FZ, Duke D, Powell CF, Zhang X, Moon S. Time-resolved X-ray radiography of sprays from engine combustion network spray a diesel injectors. Atom Sprays. 2014;24(3):251–272.

4. Griesche1 A, Zhang B, Solórzano E, Garcia-Moreno F. X-ray radiography for measuring chemical diffusion in metallic melts. Rev Sci Instr. 2010;81:056104.

5. Germer R. X-ray flash techniques. J Phys E: Sci Instrum. 1979;12:336.

6. Webster EA. Flash X-ray studies of ballistic phenomena. Proceedings Volume 0348, 15th International Congress on High Speed Photography and Photonics; 1983. https://doi.org/10.1117/12.967819.

7. McAfee JM, Asay B, Campbell AW, Ramsay JB. The deflagration-to-detonation transition in granular HMX. Los Alamos (NM): Los Alamos National Laboratory; 1991. Report No.: LA-UR-91-2103.

8. Zellner MB, Uhlig WC. Deblurring of X-radiographs acquired using 150-, 300-, and 450-kV flash X-ray systems: compensation for a finite source size. Aberdeen Proving Ground (MD): Army Research Laboratory (US); 2019 Apr. Report No.: ARL-TR-8681.

9. Wiener N. Extrapolation, interpolation, and smoothing of stationary time series. Cambridge (MA): MIT Press; 1964. ISBN 0-262-73005-7.

10. MATLAB. Ver. 9.3. R2017b. Natick (MA): The MathWorks, Inc.; 2017.

11. OriginPro 2019b. Ver. 9.6.5.169. OriginLab Corporation; 2019.

List of Symbols, Abbreviations, and Acronyms

2-D	2-dimensional
Cu	copper
ID	inner diameter
OD	outer diameter
PSF	point spread function
SNR	signal-to-noise ratio

1 (PDF) DEFENSE TECHNICAL INFORMATION CTR DTIC OCA

1 (PDF) CCDC ARL
FCDD RLD CL
TECH LIB

34 (PDF) CCDC ARL
FCDD RLW P
D LYON
S SCHOENFELD
FCDD RLW PA
S BILYK
J FLENIKEN
M MCNEIR
C WOLFE
P BERNING
M COPPINGER
W UHLIG
L VANDERHOEF
B WILMER
FCDD RLW PC
S SEGLETES
R BECKER
D CASEM
FCDD RLW PD
M KEELE
F MURPHY
C RANDOW
D KLEPONIS
A BARD
N BRUCHEY
S SCHRAML
R MUDD
R DONEY
G VUNNI
M ZELLNER
FCDD RLW PE
P SWOBODA
P BARTKOWSKI
D GALLARDY
D HORNBAKER
K KRAUTHAUSER
FCDD RLW PF
N GNIAZDOWSKI
FCDD RLW PB
C HOPPEL
FCDD RLS DP
C TIPTON
D PORSCHET

2 (PDF) PM ABCT
J ROWE
R NICOL

1 (PDF) PM BFVS
D SPENCER